Impact of cloud process in the mixing state and microphysical properties of soot particles

Fu, Yuzhen; Peng, Xiaocong; Sun, Wei; Hu, Xiaodong; Wang, Dian; Yang, Yuxiang; Guo, Ziyong; Wang, Yuanyuan; Zhang, Guohua; Zhu, Jianxi; Ou, Jie; Shi, Zongbo; Wang, Xinming; Bi, Xinhui

DOI:
10.1029/2022JD037169

Impact of Cloud Process in the Mixing State and Microphysical Properties of Soot Particles: Implications in Light Absorption Enhancement

Yuzhen Fu[1,2], Xiaocong Peng[1,2,3], Wei Sun[1,2,3], Xiaodong Hu[1,2,3], Dian Wang[1,2,3], Yuxiang Yang[1,2], Ziyong Guo[1,2,3], Yuanyuan Wang[4], Guohua Zhang[1,2,5,*], Jianxi Zhu[2,6], Jie Ou[7], Zongbo Shi[8], Xinming Wang[1,2,5], Xinhui Bi[1,2,5,*]

[1] State Key Laboratory of Organic Geochemistry and Guangdong Key Laboratory of Environmental Protection and Resources Utilization, Guangzhou Institute of Geochemistry, Chinese Academy of Sciences (CAS), Guangzhou, PR China

[2] CAS Center for Excellence in Deep Earth Science, Guangzhou, PR China

[3] University of Chinese Academy of Sciences, Beijing, PR China

[4] Department of Atmospheric Science, School of Earth Sciences, Zhejiang University, Hangzhou, PR China

[5] Guangdong-Hong Kong-Macao Joint Laboratory for Environmental Pollution and Control, Guangzhou, PR China

[6] CAS Key Laboratory of Mineralogy and Metallogeny and Guangdong Provincial Key Laboratory of Mineral Physics and Materials, Guangzhou Institute of Geochemistry, Chinese Academy of Sciences, Guangzhou, PR China

[7] Shaoguan Environmental Monitoring Center, Shaoguan, PR China

[8] School of Geography, Earth and Environmental Sciences, University of Birmingham, Birmingham, UK

*Correspondence author: Guohua Zhang (zhanggh@gig.ac.cn) and Xinhui Bi (bixh@gig.ac.cn)

Key Points:

- Cloud processing contributes to the increase of organic coating on soot aggregates, especially for those with fully embedded structure.
- The sulfate coating causes more compaction of soot aggregates than the organic coating upon cloud processing.
- Changes in the microphysical properties of soot particles driven by one cloud event increase their absorption enhancement by 1.29 times.

Abstract

The radiative forcing of soot is dependent on the morphology, mixing state and structure. Cloud processing has been predicted to affect their mixing properties but little is known about the resulting light absorption properties. We collected ambient particles in the pre-cloud period, the cloud residues and interstitials in the in-cloud period at Mt. Tianjing (southern China). The morphology parameters of soot aggregates with varying mixing materials (sulfate (S) and organics (OM)) and mixing structures were investigated by a transmission electron microscope, and their absorption cross section were calculated based on discrete dipole approximation. We found that the number contribution of soot-S decreased from 45% in the pre-cloud period to 32% in the in-cloud period, and that of soot-OM increased from 44% to 60%. Moreover, the number proportion of soot-OM with fully embedded structure increased remarkably in the in-cloud period (29%), compared with that in the pre-cloud period (3%). In addition, the soot-S aggregates became denser after in-cloud aqueous process. However, for soot-OM aggregates, the morphology remained relatively constant. The distinctly different change of soot-S and soot-OM in morphology highlights the chemically resolved reconstruction of soot morphology. Theoretical calculation further shows that the changes of soot particles in the mixing state and morphological characteristics by the cloud process resulted in the light absorption enhancement increase from 1.57 to 2.01. This study highlights that the evolution of microphysical properties upon cloud processing should also be considered in climate models to more accurately evaluate the impacts of soot particles.

Plain Language Summary

While soot particles are the main component of aerosols that produce positive radiative forcing in clouds, the impact of in-cloud processes on key factors (mixing state and microphysical property) for evaluating the optical properties of soot particles is unclear. Here, we report the detailed information on several parameters required to calculate the optical properties of soot particles, throughout the cloud events. And we found that changes in the mixing state, mixing structure, and morphology of soot particles under the influence of in-cloud processes lead to a significant light absorption enhancement. The results also highlight the role of in-cloud aqueous formation of secondary compositions in reshaping the soot particles, which has substantial implications for the climate impact of soot particles. Given that ~70% of the Earth's surface is covered by clouds, taking the mixing state and microphysical properties of soot particles into account in climate models may help constrain the contribution of soot particles to global radiative forcing.

1 Introduction

Soot, also known as black carbon (BC) or elemental carbon (EC) [Buseck et al., 2014], is deeply concerning because it has a multitude of effects on the global atmosphere and Earth's surface. It is the second largest contribution to warm the atmosphere after carbon dioxide [Jacobson, 2001]. Soot particles in the atmosphere exhibit complexity in size, composition, morphology, and mixing structure, which results in the high uncertainties in climate models when predicting their optical properties [Lack and Cappa, 2010; Liu et al., 2017a; Zhang and Mao, 2020] and CCN activity [Li et al., 2018; Liu et al., 2013].

The chemical and physical properties of soot particles are dynamic and vary with aging processes during atmospheric transport. They are sensitive to the formation of secondary components and atmospheric conditions, leading to complex and ever-changing mixing state and mixing structure of soot particles [Liu et al., 2017b; Zelenyuk et al., 2010; Zhang et al., 2018]. Fresh soot particles emitted from biomass burning and fossil fuel combustion are hydrophobic with bare-like structure, which generally shows the chain-like structure composed of several nanospheres with onion-like and graphene-like layers of carbon [Buseck et al., 2014; Li and Shao, 2009]. As the degree of aging increases, the soot aggregates are wrapped thicker and become more compact, resulting in more partly coated and/or fully embedded soot particles [China et al., 2014; China et al., 2015b; Wang et al., 2017; Xu et al., 2020], and higher absorption enhancement [Wu et al., 2018]. The mixing structure and morphology parameters of soot particles are key factors to calculate their optical properties [Adachi

et al., 2010; Cappa et al., 2012; Yu et al., 2019]. From the bare-like structure to being gradually coated by other components, the light absorption of soot particles will be significantly enhanced by factors ranging from 1 to 3.5 [Wu et al., 2018]. And, the optical properties of the bare-like soot aggregates with diverse fractal degrees are also different [Radney et al., 2014; Wang et al., 2021b]. Additionally, soot aggregates coated by various materials may redistribute after liquid-liquid phase separation (LLPS) under high relative humidity, which could lead to an inverted core-shell structure (soot aggregates are distributed in the outer layer of the two-phase particle) [Brunamonti et al., 2015]. Consequently, the core-shell model (concentric spheres composed of soot nuclei and coating) assumed in current climate models results in higher uncertainty of light absorption compared to observations, either overestimation [Cappa et al., 2012; Wu et al., 2018] or underestimation [Kelesidis et al., 2022]. Therefore, an accurate understanding of the mixing structure and morphology parameters of soot particles is crucial for the climate model to evaluate their radiative forcing.

Previous studies have shown that cloud could modify the mixing state and morphology of atmospheric particles [China et al., 2015a; Liu et al., 2018], through collision/coalescence and Brownian capture as well as aqueous reactions. The reconstruction of soot aggregates has been found in high humidity environments such as fog and cloud events [Bhandari et al., 2019; China et al., 2015a], which is affected by the mixing state of soot particles [Khalizov et al., 2009; Qiu et al., 2012; Zhang et al., 2008]. High humidity condition during cloud process can promote the formation of various species including inorganic (such as nitrate, sulfate, and ammonium) and

111 organic substances (such as oxalic acid, organosulfate) [Kim et al., 2019; Schneider et
112 al., 2017; Zhang et al., 2017b]. While the physical and chemical properties of organic
113 matter have been observed to bring about varying mixing structure and structural
114 reorganization of soot particles [Chen et al., 2020; Chen et al., 2016; Sharma et al.,
115 2018], how the cloud processing driven changes in the mixing state of soot particles
116 affects their microphysical properties is poorly understood yet.

117 In order to study the effects of cloud processes on mixing state and microphysical
118 properties of soot particles, samples during pre-cloud and in-cloud periods at a remote
119 high-altitude site in southern China were collected and analyzed. We investigated the
120 changes of morphology parameters (i.e., fractal dimension, aspect ratio, roundness, and
121 size) of soot aggregates with different mixing states and mixing structures from pre-
122 cloud to in-cloud periods. The possible influencing factors such as different coating
123 materials and mixing structures were discussed. Finally, the effect of cloud processing
124 on the light absorption of soot particles was evaluated.

125 **2 Methods**

126 **2.1 Sampling and Instrumentation**

127 A field observation focused on the cloud events was conducted from May 8 to June
128 3, 2018 at an atmospheric observation station (112°53′56″ E, 24°41′56″ N; 1690 m
129 above sea level) on the top of Mt. Tianjing. There is a pristine forest covering 273 km^2
130 and few anthropogenic emissions around the sampling site. Cloud events are prevalent
131 due to the influence of warm and humid air masses from the South China Sea [Lin et
132 al., 2019]. The cloud events investigated in this study were mainly affected by local

biogenic sources and long-range transport from the southwest air masses (**Fig. S1**). Soot particles mainly come from combustion activities in Southeast Asia and industrial emissions in the urban agglomeration of southern China [Zhang et al., 2017a].

A ground-based counterflow virtual impactor (GCVI, model 1205, Brechtel Mfg. Inc., USA) was used to introduce cloud droplets larger than 7.5 μm into the subsequent system [Shingler et al., 2012]. During cloud processes, cloud droplets and unactivated particles are introduced into the inlet of the GCVI, a wind tunnel, which can accelerate droplets or particles to 100 m s^{-1}. The flow rate of the filtered and heated add-flow can be adjusted in the range of 16-23 L min^{-1} to ensure the cut size of 7.5 μm with the transmission efficiency of 50%. The flow rate of sample-flow is kept at a constant 15 L min^{-1} for multiple instruments downstream. The cloud droplets went through an evaporation chamber (40 ℃) to remove the associated water, leaving the cloud residual (RES) particles for the follow-up particle sampling or on-line analysis. The add-flow with high temperature indirectly controls the sample-flow temperature of evaporation chamber. Some semi-volatile organic compounds will be lost under heating, and the loss at 40 ℃ may be less than 1% [Cao et al., 2018]. In addition, a $PM_{2.5}$ cyclone inlet followed by a silica gel diffusion dryer was used for the collection of inactivated interstitial (INT) particles during the cloud events and the ambient particles during free-cloud periods.

A DKL-2 sampler (Genstar Electronic Technology Co., Ltd., China) employing a single-stage cascade impactor with a 0.5 mm diameter jet nozzle was used to collect individual particles on copper grids coated by carbon film (300 mesh, Beijing

155 Zhongjingkeyi Technology Co., Ltd., China) with the airflow of 1 L min^{-1}. The effective
156 size d_{50} is 0.5 μm for particles with a density of 2 g cm^{-3}. The DKL-2 sampler was
157 described in detail by Li et al. [2011]. The sampling duration varied from 5 to 10 min
158 based on the number concentration of particles. After collecting, samples were stored
159 in a sealed plastic box and placed in a desiccator (RH (relative humidity) < 30%) at 25 ℃
160 for later analysis.

161 A transmission electron microscope (TEM, FEI Talos F200S, USA) operated at
162 200 kV was used to observe the morphology of particles on the copper grids, which
163 was coupled with an energy-dispersive X-ray spectrometer (EDS) to obtain the
164 elemental composition including carbon and heavier elements ($Z \geq 6$). The distribution
165 of particles on the copper grids is not uniform. The diameter of particles distributed in
166 the center is larger than that in the edge. Therefore, in order to ensure that particles
167 analyzed are representative within the entire particle size range, 3-4 areas were selected
168 from the center to the edge on each copper grid. The electron beam of TEM was focused
169 on the particles when the soot aggregates were coated. The components with weak
170 thermal stability were lost under the electron beam, but the refractory components
171 remain unchanged, so the morphology of soot aggregates could be clearly captured (**Fig.**
172 **S2**). An image analysis software, ImageJ (https://imagej.nih.gov/), was used to obtain
173 the morphology parameters of all particles by analyzing TEM images.

174 During the observation period, the mass concentrations of $PM_{2.5}$, O_3, SO_2 and NO_X
175 were monitored in real time by tapered element oscillating microbalance (TEOM 1405,
176 Thermo Fisher Scientific Inc., MA, US), O_3 analyzer (Model 49i, Thermo Fischer

Scientific Inc., USA), pulsed UV fluorescence (Model 43i-TLE, Thermo Fischer Scientific Inc., USA), and NO-NO_2-NO_X analyzer (Model 42i-TL, Thermo Fischer Scientific Inc., USA), with details described elsewhere [Gong et al., 2018].

2.2 Division of cloud periods and meteorological characteristics

This field observation spanned two complete non-precipitation cloud processes, which were named as cloud events #1 and #2. Both cloud events formed at night and dissipated at noon of the next day. During the cloud events, prevailing wind direction was from the southwest, and wind speed was in the range of 4.1-9.4 m s^{-1}. The mass concentration of $PM_{2.5}$ was 2-23 μg m^{-3} during cloud event #1 and 4-47 μg m^{-3} during cloud event #2. Two periods were defined according to the visibility (*Vis*) and RH [Lin et al., 2019]: pre-cloud period (*Vis* > 3 km or RH < 95%) and in-cloud period (*Vis* ≤ 3 km and RH ≥ 95%) (**Fig. S3**). Due to rapid development of formation and dissipation of cloud, INT particles were only collected in the stability period with low visibility (*Vis* < 0.1 km) and the mass concentration of $PM_{2.5}$ (< 5 μg m^{-3}) [Yang et al., 2021]. The average visibility and RH during the stability period of cloud processes were 38 ± 13 m and 100 ± 0.2 %, which were 600 ± 890 m and 99 ± 0.7 % in the non-stability (formation and dissipation) period respectively. In the following text, particles in the in-cloud period refer to all the RES particles during cloud processes, except as specifically noted. Overall, 4569 particles were analyzed by TEM/EDS including 1188 particles in the pre-cloud period and 3381 particles in the in-cloud period. Standard errors for the number fraction of particles were estimated assuming Poisson distribution [Pratt et al., 2010].

During two periods of cloud event #1, there was little change for the concentrations of SO_2 and O_3 in the atmosphere. Differently, they changed dramatically during cloud event #2. The average concentrations of SO_2 and O_3 reduced from 3.1 μg m^{-3} and 188.2 μg m^{-3} in the pre-cloud period to 1.5 μg m^{-3} and 82.1 μg m^{-3} in the in-cloud period, respectively. Due to the cloud scavenging of particulate matter, the average concentration of $PM_{2.5}$ was significantly reduced from 20.4 μg m^{-3} in the pre-cloud period and to 5.1 μg m^{-3} during the in-cloud period for cloud event #1 and from 32.7 μg m^{-3} to 12.3 μg m^{-3} for cloud event #2. The average concentration of NO_X was higher during cloud event #2 (10.5 μg m^{-3}) than cloud event #1 (3.8 μg m^{-3}).

2.3 The calculation of morphology parameters of soot aggregates

Fractal dimension (D_f) is a morphology parameter used to characterize the mass-based fractal properties, which can quantify the fractal degree of soot aggregates [Samson et al., 1987]. Brasil et al. [1999] linked the structural properties between computer-simulated three-dimensional aggregates and their two-dimensional projection images, which can be used to infer morphology parameters (such as D_f) of three-dimensional aggregates from analysis of two-dimensional electron microscopy images. This method has been frequently used in the calculation of soot aggregates morphology parameters [Wang et al., 2017; Wentzel et al., 2003]. The D_f follows the statistical scaling law:

$$\mathrm{N} = k_g \left(\frac{2R_g}{d_p}\right)^{D_f} \quad (1)$$

where N and d_p represent the number and average diameter of monomers within a certain soot aggregate, respectively. R_g refers to the gyration radius of the soot aggregate, and k_g is the fractal pre-factor. The calculation method of D_f is described in detail in the supporting information (Text S1). Aspect ratio (AR) and roundness (RN) are also calculated to quantify the morphology of soot aggregates, which can be obtained by equations (2) and (3):

$$\mathrm{AR} = \frac{L_{max}}{W_{max}} \tag{2}$$

$$\mathrm{RN} = \frac{4A_a}{(\pi {L_{max}}^2)} \tag{3}$$

where L_{max} and W_{max} are the maximum length and width of a bounding box. A_a is the projected area of the soot aggregate. For a spherical particle: $D_f = 3$, and AR = RN = 1. For a nonspherical particle: 1 (linear particle) $\leq D_f < 3$, AR > 1, and RN < 1. In addition, the equivalent area diameter (D_{eq}) represents the size of particle, which can be obtained by equation (4).

$$D_{eq} = \sqrt{\frac{4A_a}{\pi}} \tag{4}$$

2.4 The calculation of optical properties of soot particles

The absorption, scattering and extinction cross sections of soot particles at 532 nm were calculated by discrete dipole approximation (DDA) (http://ddscat.wikidot.com/), which has been widely applied to calculate the optical properties of soot particles with different coating materials and mixing structures [Draine and Flatau, 1994]. The input parameters are refractive index of material, the shape and effective radius of particle (D_f, N, d_p). The refractive indices are 1.76+0.63i, 1.53+0i and 1.48+0i for soot

aggregate, sulfate coating and organic coating, respectively [Luo et al., 2019; Nakayama et al., 2010; Worringen et al., 2008]. Shape and effective radius can be obtained based on the images from TEM. Absorption enhancement (E_{abs}) is the ratio of C_{abs} (absorption cross section) of soot particles to soot aggregates, which is described in detail in the supporting information. In this study, the Electron-Microscope-to-BC-Simulation (EMBS) tool, recently developed by Wang et al. [2021b], was applied to build realistic soot shape models with diverse morphology and mixing structures. The average number and diameter of monomers of soot aggregates in the pre-cloud and in-cloud periods are 96, 102 and 45 nm, 44 nm, respectively. So soot aggregate is defined as 100 monomers with the diameter of 44 nm in the theoretical calculation. The variation of E_{abs} with the number of monomers is less than 3% (**Fig. S4**).

3 Results and discussions

3.1 The impact of cloud process on the mixing state and structure of soot particles

Three components were identified within soot particles based on element composition and morphology, including soot, sulfate and organic matter [Li et al., 2016]. Soot was identified by chain-like structure in morphology and abundant carbon in elemental composition. Organic matter exhibited spherical or irregular shape with abundant C and minor O. Sulfate was dominated by S and O, and some were accompanied by a small amount of N, K and Na. It is often bubbly appearance due to the loss of volatile materials (such as ammonium nitrate) by high-energy electron beams during TEM/EDS analysis. Therefore, the inorganic component is identified according to the bubble-shape and S-peak, so sulfate represent inorganic components here. Soot

particles contributed to 12-26% of all analyzed particles by number, which were divided into three classes based on the mixing materials directly contacting with soot aggregates (soot fraction in the whole particle), including bare-like soot aggregate with negligible coating (**Fig. 1a**), soot aggregate coated by sulfate (soot-S) (**Fig. 1b, c, d**), or by organic matter (soot-OM) (**Fig. 1e, f**). Such a classification stresses chemical components in direct contact with soot aggregates, which is slightly different from the classification based on the mixing state of the whole particle [Yuan et al., 2019]. According to various mixing structures between soot aggregates and other materials, soot particles were divided into four classes (**Fig. 1**), including bare-like (**Fig. 1a**), attached (**Fig. 1b**), partly coated (**Fig. 1c**), and fully embedded (**Fig. 1d-f**) [China et al., 2013; Liu et al., 2015]. Attached soot particle was soot aggregate adhering to the surface of the host particle. Partly coated and fully embedded soot particles referred to part and full of soot aggregate wrapped by other materials. Given the limited number of soot particles and similar air mass sources of two cloud events, the following results and discussions are based on a merged dataset from two cloud events.

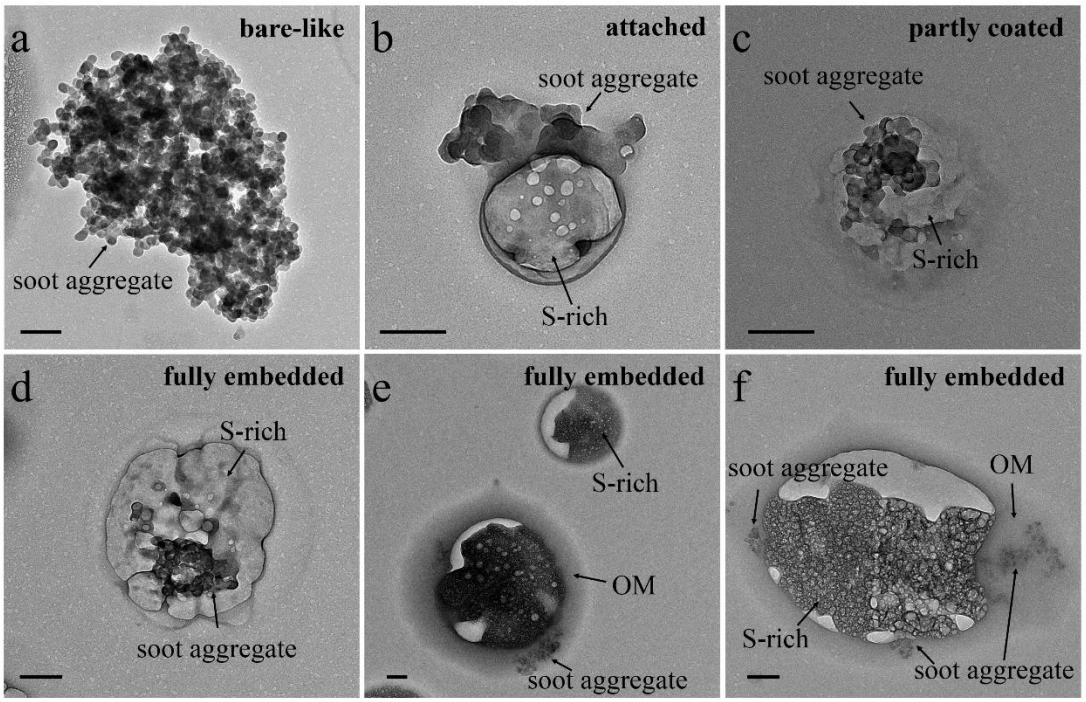

Figure 1. TEM images of soot particles with different mixing structures including bare-like (a), attached (b), partly coated (c) and fully embedded (d-f). The scale in the images is 200 nm.

It can be seen in **Fig. 2** that mixing states and structures of soot particles exhibit distinctly different characteristics between the pre-cloud and in-cloud periods. Soot-OM particles have a higher fraction in the in-cloud period (60 ±2.6%) than that in the pre-cloud period (44 ±5.1%), but soot-S particles account for lower proportion in the in-cloud period (31 ±3.7%) than pre-cloud period (45 ±5.1%). Compared with pre-cloud period, the proportion of soot particles with fully embedded structure in the in-cloud period shows a considerable increase (from 14 ±2.8% to 38 ±2.9%). Specifically, the proportion of soot particles fully embedded in OM, which increase from 3 ±1.3% in the pre-cloud period to 29 ±2.6% in the in-cloud period. Soot particles with partly coated structure reduce from 54 ±5.7% in the pre-cloud period to 37 ±2.9% in the in-

cloud period. The contribution of bare-like and attached soot particles is lower, ranging from 9 ±1.4% to 21 ±3.4%. The proportion of soot particles with LLPS was 2 ±1.0% and 11 ±1.6% in the pre-cloud and in-cloud period respectively, which were mainly completely coated by OM (**Fig. 1e-f**).

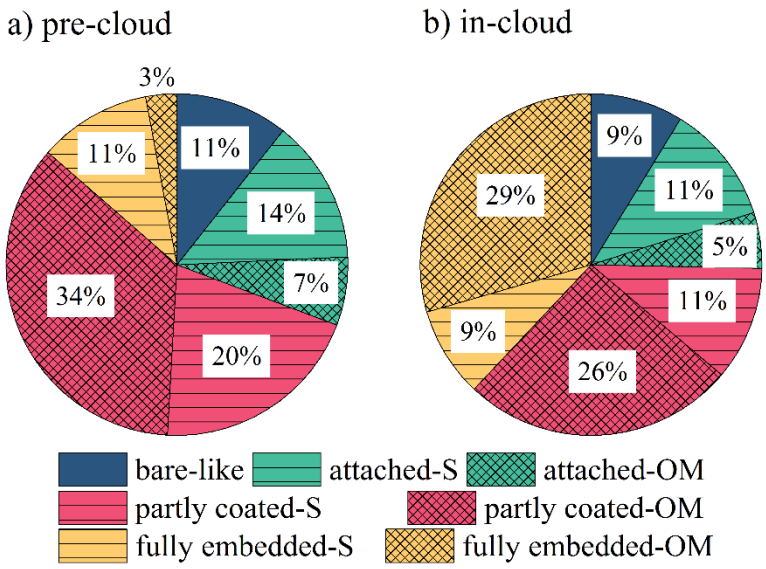

Figure 2. The number fraction of soot particles with different mixing structures coated by sulfate (soot-S) or organics (soot-OM) in the pre-cloud and in-cloud periods.

The increase of soot-OM fraction in the in-cloud period is most likely attributed to the cloud processing involving abundance of ozone and volatile organic compounds (VOCs) [Lv et al., 2019; Wang et al., 2021c], which may also be attributed to the preferential activation of soot-OM particles, but it is unlikely important. As observed by Zhang et al. [2017a] at the same site, soot-OM particles are less activated than soot-S particles. More soot-OM particles than soot-S particles during the in-cloud period may be related to LLPS, in which the soot aggregates are distributed in the organic phase with similar polarity rather than inorganic phase [Brunamonti et al., 2015]. Furthermore, as shown in **Fig. 3**, from the pre-cloud to in-cloud period, the average

coated fraction (F, the area ratio of soot aggregate embedded in host particle to soot aggregate) increased from 46 ± 15% to 67 ± 14% for soot particles with partly coated structure, and average relative coating thickness (D_p/D_c, the diameter ratio between particle and soot aggregate) increased from 2.3 ± 1.2 to 4.4 ± 3.6 for soot particles with fully embedded structure. Consistently, the average D_{eq} of soot particles increased from 845 ± 417 nm to 1214 ± 898 nm after cloud processing. The increase of F, D_p/D_c and D_{eq} indicates that soot aggregates obtain thicker coating due to cloud processing.

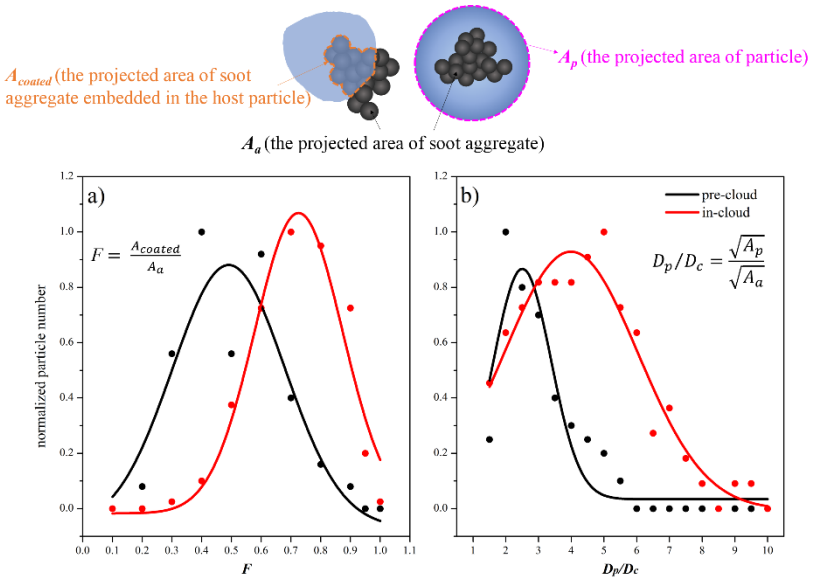

Figure 3. The distribution of F ($0 < F < 1$) for partly coated soot particles (a) and D_p/D_c (> 1) for fully embedded soot particles (b) in the pre-cloud and in-cloud periods. With the increase of F and D_p/D_c, the volume ratio of the coated soot aggregates is higher, and the coating layer is thicker.

315 ### 3.2 The impact of cloud process on the morphology of soot aggregates

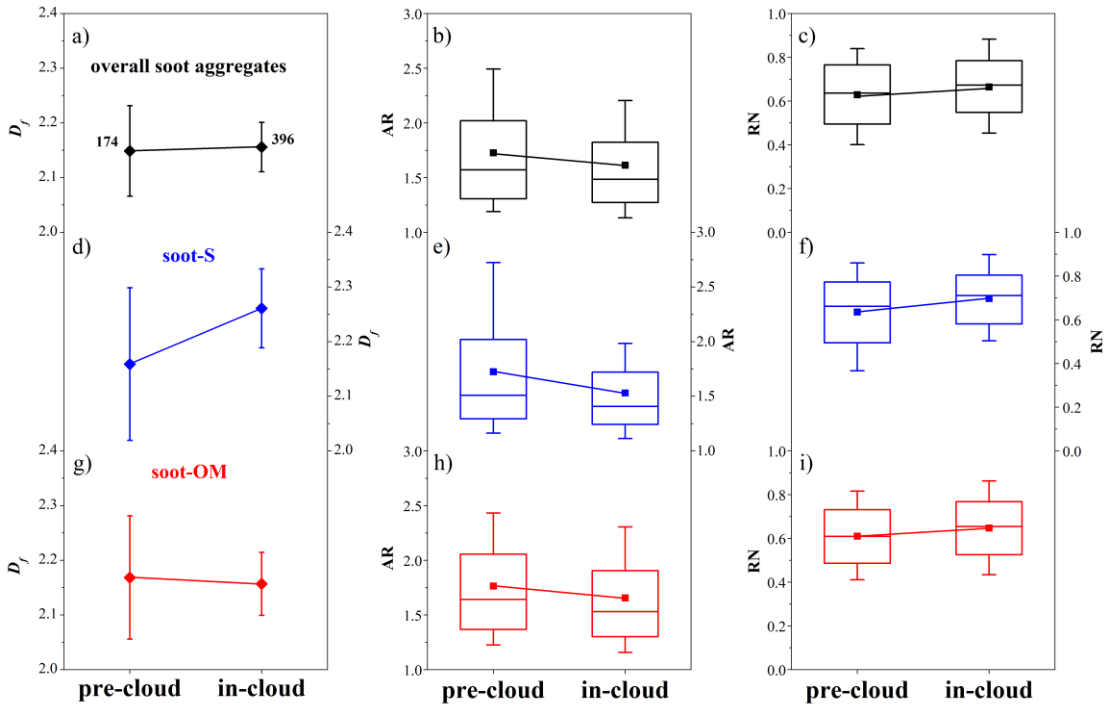

316

317 **Figure 4.** The D_f (a, d, g), AR (b, e, h) and RN (c, f, i) of soot aggregates including
318 overall soot aggregates, soot-S and soot-OM in the pre-cloud and in-cloud period. The
319 number (a) is the amount of soot aggregates used to calculate the morphology
320 parameters. D_f error bars are the error in the fitting of N and $2R_g/d_p$ when calculating D_f.
321 Box and whisker plot shows lower, median, and upper lines, denoting the 25th, 50th,
322 and 75th percentiles, respectively; the lower and upper edges denote the 10th and 90th
323 percentiles, respectively.

324 The morphology parameters of overall soot aggregates, including D_f, AR and RN,
325 show a limited change from the pre-cloud to in-cloud period (**Fig. 4**). Consistently, the
326 RES and INT soot aggregates during the stability period of cloud process also exhibit
327 similar morphology with similar D_f, AR, and RN (**Fig. S5**). The above result indicates
328 limited restructuring of soot aggregates upon cloud processing, which is inconsistent

329 with previous studies reporting that high humidity condition facilitates the restructuring
330 of soot aggregates [Qiu et al., 2012; Zhang et al., 2008], leading to larger D_f and RN,
331 and lower AR.

332 Such inconsistency might be attributed to the chemically resolved reconstruction
333 of soot aggregates due to cloud processing. As shown in **Fig. 4**, the D_f of soot-S
334 aggregates was 2.16 ± 0.14 in the pre-cloud period, and increased to 2.26 ± 0.07 in the
335 in-cloud period. Differently, the D_f of soot-OM aggregates between the pre-cloud and
336 in-cloud periods were quite similar (2.17 ± 0.11 and 2.16 ± 0.06). Similar trend was
337 also observed for the AR and RN of soot aggregates (**Fig. 4**), with larger changes of AR
338 and RN for soot-S aggregates from the pre-cloud to in-cloud periods. Such difference
339 indicates that organics lead to less compaction of soot aggregates, rather than sulfate.
340 The restructure of soot aggregates depends on the uptake of water by the coating
341 materials [Guo et al., 2016], and the following evaporation of water [Enekwizu et al.,
342 2021; Ma et al., 2013]. Complete encapsulation of organic coating produces lower
343 surface tension than partly coated structure and sulfate coating during water evaporation
344 [Schnitzler et al., 2017], resulting in less degree of reconstruction between monomers
345 of soot aggregates fully embedded in organics. Such phenomenon is similar to that
346 reported by Cross et al. [2010], who found that sulfuric acid coating caused a more
347 compact shape of soot aggregates than DOS (dioctyl sebacate) coating in laboratory
348 experiments. Therefore, with the increase contribution of soot-OM in the in-cloud
349 period, in particular the fully embedded structure (> 50%) (**Fig. 2**), the overall soot
350 aggregates show similar morphology parameters between pre-cloud and in-cloud

period.

The differences in morphology, mixing state and mixing structure from the inactivated INT to activated RES particles during the stability period of cloud events can also support the above hypothesis. The proportion of soot-OM in the RES particles (68 ± 4.6%) was higher than that in the INT particles (48 ± 7.1%), and the proportion of soot-OM particles with fully embedded structure in the RES particles (37 ± 3.4%) was about 4 times that in the INT particles (9 ± 3.5%) (**Fig. S6**). Furthermore, the D_f of soot-OM aggregates in the in-cloud period was smaller than that of the soot-S aggregates for the RES particles. Higher proportions and lower D_f value of soot-OM aggregates lead to the limited change in the morphology of overall soot aggregates between the RES and INT particles. Our previous study also found a phenomenon inconsistent with the general concept that lower D_f of soot aggregates in the RES particles than that in the INT particles at the same site [Fu et al., 2020], which is most likely due to the higher fraction of soot-OM in the RES particles (58 ± 6.2%) than that in the INT particles (28 ± 5.0%).

3.3 Effect of cloud processing in light absorption of soot particles

Fig. 5 shows the E_{abs} of soot particles in the pre-cloud and in-cloud periods, based on the observed morphology, mixing state, and mixing structure. In order to illustrate the changes in the light absorption of soot particles within a representative size range upon cloud processing, five groups of D_p/D_c were selected, ranging from 1.5 to 3.9 in the pre-cloud period and from 3.1 to 5.5 in the in-cloud period (**Table S1**). The selection of the D_p/D_c range is based on the observed particles, as detailed in the supporting

information (Text S3). For bare-like soot particles, the D_f of soot-S aggregates increases from 2.16 ±0.14 in the pre-cloud period to 2.26 ±0.07 in the in-cloud period, resulting in a limited absorption enhancement with the E_{abs} of 1.02. As reported elsewhere, the enhancement of light absorption of soot particles with attached structures is limited (E_{abs} < 1.1) [Adachi and Buseck, 2013; Schnaiter et al., 2003; Wang et al., 2021b]. Differently, the light absorption increased significantly for soot particles with partly coated and fully embedded structures (**Fig. 5a, b**), associated with the increase of coating degree including coated fraction and thickness [Adachi et al., 2010; Guo et al., 2016]. With the increase of F and D_p/D_c after cloud processing, E_{abs} are 1.76 ±0.29 in the pre-cloud period and 2.36 ±0.38 in the in-cloud period for soot particles with partly coated structure. For soot particles with fully embedded structure, E_{abs} are 2.35 ±0.28 in the pre-cloud period and 2.63 ±0.08 in the in-cloud period. The E_{abs} of soot particles with LLPS was 1.78 ± 0.14 and 1.93 ± 0.07 in the pre-cloud and in-cloud period respectively, which was smaller than that of soot particles without LLPS, with an average of 26% over different D_p/D_c (**Fig. S8**). The E_{abs} of soot particles with different mixing structures vary greatly, which may be one of the reasons for the lower E_{abs} of soot particles in some field investigation cases [Cappa et al., 2012; Fu et al., 2021], that is, the attached and partly coated structures soot particles may account for the main proportion. In the pre-cloud period, the average E_{abs} of partly coated soot particles (1.76 ±0.29) and the average E_{abs} of fully embedded soot particles (2.35 ±0.28) were both within the range reported by current laboratory studies (1-1.9 for partly coated structure and 2.2-2.5 for fully embedded structure) [Chakrabarty and Heinson, 2018; Scarnato et

al., 2013], which were lower than the average E_{abs} of soot particles with partly coated (2.36 ± 0.38) and fully embedded (2.63 ± 0.08) structure in the in-cloud period. Additionally, the E_{abs} of soot-S and soot-OM particles with different mixing structures, F and D_p/D_c is in the range of 1.0-2.7 and 1.0-3.0 respectively, which is consistent with previous studies [Peng et al., 2016; Schnaiter et al., 2003; Schnaiter et al., 2005].

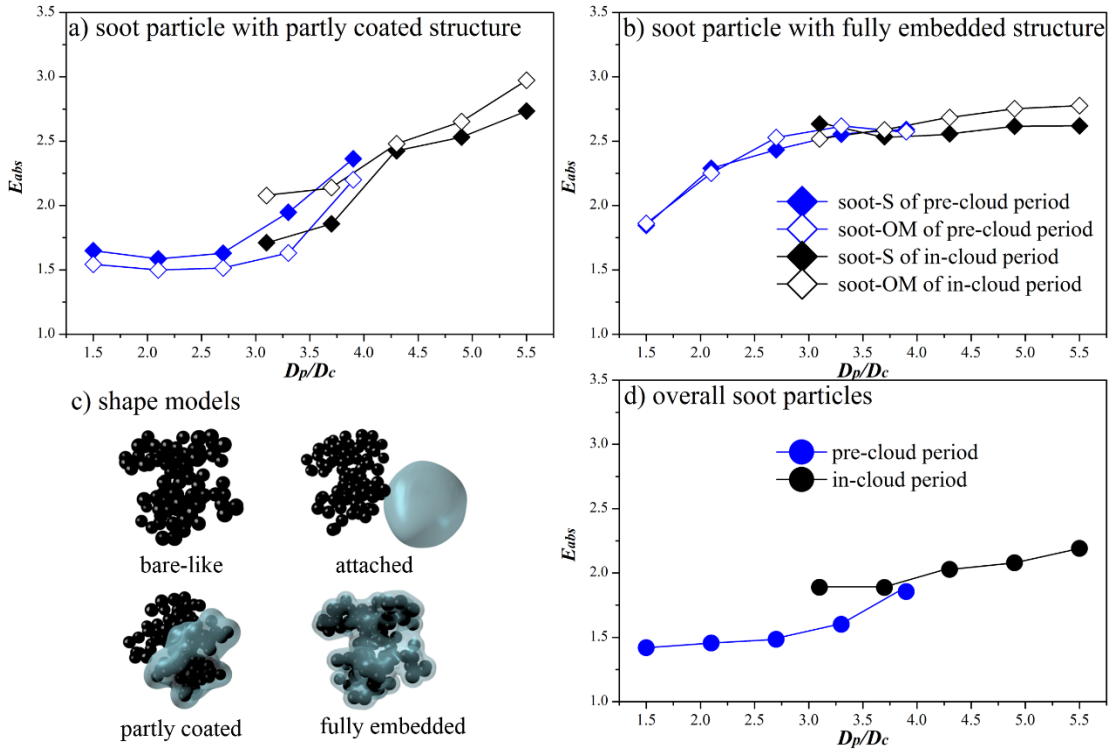

Figure 5. Shape models of soot particles with different mixing structures, and E_{abs} of soot particles in the pre-cloud and in-cloud periods.

For the overall soot particles, the cloud process likely induces a pronounced increase of light absorption based on theoretical calculations. Corresponding to the changes in the proportion of soot particles with various mixing states and structures upon cloud processing, the E_{abs} of all soot particles increased from 1.57 ± 0.16 in the pre-cloud period to 2.01 ± 0.12 in the in-cloud period (**Fig. 5d**), and the cloud process

408 resulted in a factor of 1.29 ± 0.06 increase in E_{abs}. Our calculated E_{abs} of soot particles
409 in the pre-cloud period is higher than that in urban areas [Healy et al., 2015; Lan et al.,
410 2013; Nakayama et al., 2014], which may be due to the higher degree of aging of the
411 soot particles at this remote site. Higher E_{abs} of soot particles (2.1) has also been
412 observed at the cloudy Mt. Tai in northern China [Wang et al., 2021a]. As indicated by
413 Peng et al. [2016], the E_{abs} of soot particles could increase by a factor of 2.4 after several
414 hour's aging in polluted urban air. Our study indicates that cloud processing during one
415 event could increase the E_{abs} of soot particles by 1.29 times, which underlines the
416 potential effect of cloud on rapid aging of soot particles.

417 **3.4 A conceptual model for the impact on the mixing state and microphysical**
418 **properties of soot particles of cloud process**

419 We came up with a conceptual model, as illustrated in **Fig. 6**, to reflect the changes
420 of mixing state and microphysical properties of soot particles from the pre-cloud to in-
421 cloud period. In the pre-cloud period, soot particles come from long-range transport
422 and are mainly partly coated. Aged soot particles would be activated and grow into
423 cloud droplets during cloud events. The mixing structure of soot particles is expected
424 to change since the water-soluble components mixed with the soot aggregates will be
425 dissolved in the cloud droplets. In addition, secondary organic compositions could also
426 be formed through uptake and aqueous processing of VOCs [Fu et al., 2020; Zhang et
427 al., 2017a]. After the evaporation of cloud droplets, LLPS occurs and would lead to
428 two-phase solid particles composed of outer organic phase and inner inorganic phase
429 [Shiraiwa et al., 2013], and soot aggregates will redistribute in organic phase with

similar polarity. Although not emphasized, the soot aggregates have been found to be dominantly embedded in the organic phase in the remote region [Yu et al., 2019], with a large fraction (61%) of soot-OM aggregates distributed in outer organic phase likely due to cloud processing. The production of organic matter in cloud and the occurrence of LLPS correspond to the significant increase of soot-OM particles with fully embedded structure, which would significantly enhance the light absorption of soot particles.

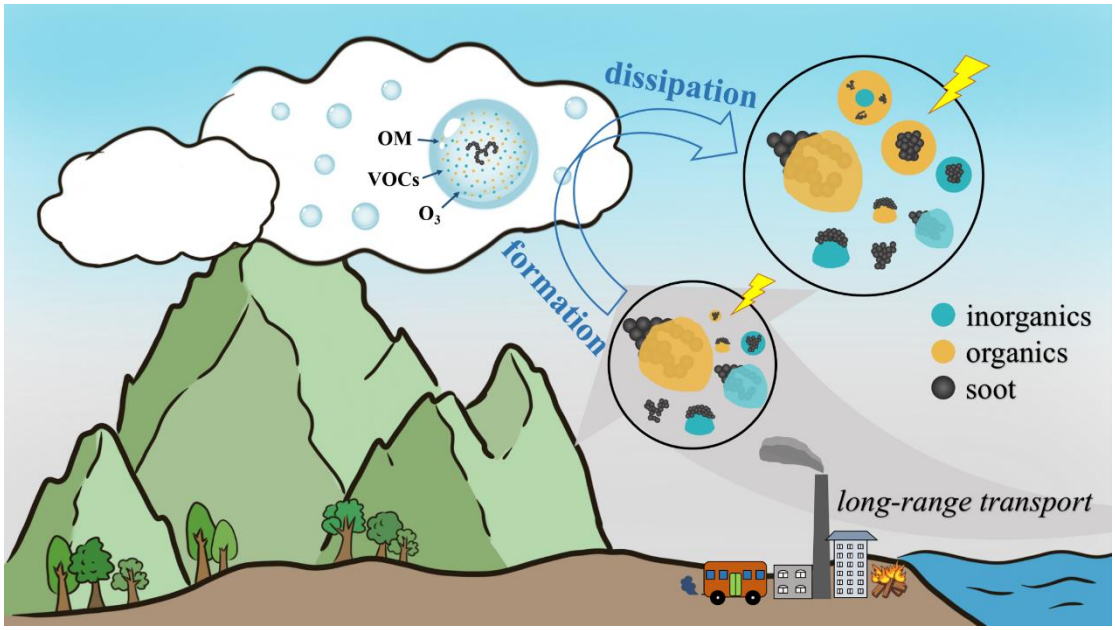

Figure 6. Schematic diagram showing the change in morphology, mixing state, and mixing structure of soot particles throughout cloud processing.

4 Atmospheric implications and conclusions

This study emphasizes that it is necessary to consider the encapsulating materials and mixing structures for better understanding of the impact of cloud on soot particles. Attributed to cloud processing, the soot-S aggregates become more compact, while the soot-OM aggregates do not. Meanwhile, the changes in morphology of soot aggregates,

445 mixing state and mixing structure of soot particles driven by cloud processing would
446 have substantial implications for the optical properties of soot particles. Theoretical
447 calculation shows that the E_{abs} of soot-particles processed by cloud is as high as 2.01 ±
448 0.12, which is 1.29 ± 0.06 times that of the pre-cloud period. Given that clouds cover
449 nearly 70% of the Earth [King et al., 2013], such a significant increase in E_{abs} indicates
450 that cloud processing may represent a critical factor, which has not been revealed in the
451 evolution of light absorption of soot. The results also support the significance of
452 morphology, mixing state and mixing structure of soot particles in model calculations
453 to evaluate the climate impact of soot particles [Penner et al., 2006; Zhuang et al., 2010].
454 While such information is accounted for in particle-resolved aerosol model [Fierce et
455 al., 2020], it is still not considered in most climate models [Cooke and Wilson, 1996;
456 Park et al., 2011; Zhang et al., 2019]. In addition, field observations found high
457 uncertainty in the abundance of soot particles in ice clouds [Cozic et al., 2008;
458 Kupiszewski et al., 2016]. Our observations indicate that the morphological evolution
459 of soot aggregates due to warm cloud processing was mainly driven by the coating of
460 organic compounds, which may have potential influence on the ice nucleation activities
461 [Nichman et al., 2019]. Laboratory simulation experiments have shown a significant
462 enhancement of ice nucleation activity of soot particles processed by cloud, most likely
463 attributed to the modification of morphology by cloud processing [Mahrt et al., 2020].
464 Our results at the remote site surrounded by a large area of forest may represent the
465 mixing state and morphological characteristics of soot particles in the area with
466 significant biogenic VOCs precursors, and thus can be used as a reference for the

467 climate model to access the climatic impact of soot particles in similar regions.

468 **Acknowledgements**

469 This work was funded by the Natural Science Foundation of Guangdong Province
470 (2019B151502022), National Natural Science Foundation of China (42192514,
471 42077322, and 41877307), Youth Innovation Promotion Association CAS (2021354),
472 and Guangdong Foundation for Program of Science and Technology Research
473 (2020B1212060053).

474 **Conflict of Interest**

475 There are no conflicts of interest in the article.

476 **Data Availability Statement**

477 Data supporting the results are available in the supporting information. The
478 processed data presented in this paper are available on Zenodo
479 (https://doi.org/10.5281/zenodo.7073072) [Fu et al., 2022], including the number
480 fraction of soot particles with different mixing states and structures, the distribution of
481 F and D_p/D_c, morphology parameters of soot aggregates, and E_{abs} of soot particles in
482 the pre-cloud and in-cloud periods. The back trajectories data are calculated with hybrid
483 single-particle Lagrangian integrated trajectory model
484 (https://www.ready.noaa.gov/HYSPLIT_hytrial.php) [NOAA, 2022]. The source code
485 of EMBS is from Wang et al. [2021b]. The source code of DDA developed by Bruce T.
486 Draine and Piotr J. Flatau, and the version used in this study is DDSCAT 7.3.3, which
487 can be obtained online (http://ddscat.wikidot.com/) [Draine and Flatau, 2019].

References

Adachi, K., and P. R. Buseck (2013), Changes of ns-soot mixing states and shapes in an urban area during CalNex, *Journal of Geophysical Research-Atmospheres*, *118*(9), 3723-3730, doi:10.1002/jgrd.50321.

Adachi, K., S. H. Chung, and P. R. Buseck (2010), Shapes of soot aerosol particles and implications for their effects on climate, *Journal of Geophysical Research-Atmospheres*, *115*, D15206, doi:10.1029/2009jd012868.

Bhandari, J., et al. (2019), Extensive Soot Compaction by Cloud Processing from Laboratory and Field Observations, *Scientific reports*, *9*(1), 11824-11824, doi:10.1038/s41598-019-48143-y.

Brasil, A. M., T. L. Farias, and M. G. Carvalho (1999), A recipe for image characterization of fractal-like aggregates, *Journal of Aerosol Science*, *30*(10), 1379-1389, doi:10.1016/s0021-8502(99)00026-9.

Brunamonti, S., U. K. Krieger, C. Marcolli, and T. Peter (2015), Redistribution of black carbon in aerosol particles undergoing liquid-liquid phase separation, *Geophysical Research Letters*, *42*(7), 2532-2539, doi:10.1002/2014gl062908.

Buseck, P. R., K. Adachi, G. Andras, E. Tompa, and P. Mihaly (2014), Ns-Soot: A Material-Based Term for Strongly Light-Absorbing Carbonaceous Particles, *Aerosol Science and Technology*, *48*(7), 777-788, doi:10.1080/02786826.2014.919374.

Cao, L.-M., X.-F. Huang, Y.-Y. Li, M. Hu, and L.-Y. He (2018), Volatility measurement of atmospheric submicron aerosols in an urban atmosphere in southern China, *Atmospheric Chemistry and Physics*, *18*(3), 1729-1743, doi:10.5194/acp-18-1729-2018.

510 Cappa, C. D., et al. (2012), Radiative Absorption Enhancements Due to the Mixing
511 State of Atmospheric Black Carbon, *Science*, *337*(6098), 1078-1081,
512 doi:10.1126/science.1223447.
513 Chakrabarty, R. K., and W. R. Heinson (2018), Scaling Laws for Light Absorption
514 Enhancement Due to Nonrefractory Coating of Atmospheric Black Carbon Aerosol,
515 *Physical Review Letters*, *121*(21), doi:10.1103/PhysRevLett.121.218701.
516 Chen, C., O. Y. Enekwizu, X. Ma, Y. Jiang, A. F. Khalizov, J. Zheng, and Y. Ma (2020),
517 Effect of organic coatings derived from the OH-initiated oxidation of amines on soot
518 morphology and cloud activation, *Atmospheric Research*, *239*, 104905,
519 doi:10.1016/j.atmosres.2020.104905.
520 Chen, C., X. Fan, T. Shaltout, C. Qiu, Y. Ma, A. Goldman, and A. F. Khalizov (2016),
521 An unexpected restructuring of combustion soot aggregates by subnanometer coatings
522 of polycyclic aromatic hydrocarbons, *Geophysical Research Letters*, *43*(20), 11080-
523 11088, doi:10.1002/2016gl070877.
524 China, S., et al. (2015a), Morphology of diesel soot residuals from supercooled water
525 droplets and ice crystals: implications for optical properties, *Environmental Research*
526 *Letters*, *10*(11), 114010, doi:10.1088/1748-9326/10/11/114010.
527 China, S., C. Mazzoleni, K. Gorkowski, A. C. Aiken, and M. K. Dubey (2013),
528 Morphology and mixing state of individual freshly emitted wildfire carbonaceous
529 particles, *Nature Communications*, *4*, 2122, doi:10.1038/ncomms3122.
530 China, S., N. Salvadori, and C. Mazzoleni (2014), Effect of Traffic and Driving
531 Characteristics on Morphology of Atmospheric Soot Particles at Freeway On-Ramps,

Environmental Science & Technology, *48*(6), 3128-3135, doi:10.1021/es405178n.

China, S., et al. (2015b), Morphology and mixing state of aged soot particles at a remote marine free troposphere site: Implications for optical properties, *Geophysical Research Letters*, *42*(4), 1243-1250, doi:10.1002/2014gl062404.

Cooke, W. F., and J. J. N. Wilson (1996), A global black carbon aerosol model, *Journal of Geophysical Research-Atmospheres*, *101*(D14), 19395-19409, doi:10.1029/96jd00671.

Cozic, J., S. Mertes, B. Verheggen, D. J. Cziczo, S. J. Gallavardin, S. Walter, U. Baltensperger, and E. Weingartner (2008), Black carbon enrichment in atmospheric ice particle residuals observed in lower tropospheric mixed phase clouds, *Journal of Geophysical Research-Atmospheres*, *113*(D15), doi:10.1029/2007jd009266.

Cross, E. S., et al. (2010), Soot Particle Studies-Instrument Inter-Comparison-Project Overview, *Aerosol Science and Technology*, *44*(8), 592-611, doi:10.1080/02786826.2010.482113.

Draine, B. T., and P. J. Flatau (1994), DISCRETE-DIPOLE APPROXIMATION FOR SCATTERING CALCULATIONS, *Journal of the Optical Society of America a-Optics Image Science and Vision*, *11*(4), 1491-1499, doi:10.1364/josaa.11.001491.

Draine, B. T., and P. J. Flatau (2019), Discrete Dipole Scattering (DDSCAT) [Software]. http://ddscat.wikidot.com/.

Enekwizu, O. Y., A. Hasani, and A. F. Khalizov (2021), Vapor Condensation and Coating Evaporation Are Both Responsible for Soot Aggregate Restructuring, *Environmental Science & Technology*, *55*(13), 8622-8630, doi:10.1021/acs.est.1c02391.

554 Fierce, L., et al. (2020), Radiative absorption enhancements by black carbon controlled
555 by particle-to-particle heterogeneity in composition, *Proceedings of the National*
556 *Academy of Sciences of the United States of America*, *117*(10), 5196-5203,
557 doi:10.1073/pnas.1919723117.
558 Fu, Y., et al. (2020), Impact of in-cloud aqueous processes on the chemical
559 compositions and morphology of individual atmospheric aerosols, *Atmospheric*
560 *Chemistry and Physics*, *20*(22), 14063-14075, doi:10.5194/acp-20-14063-2020.
561 Fu, Y., et al. (2021), Filter-based absorption enhancement measurement for internally
562 mixed black carbon particles over southern China, *Science of The Total Environment*,
563 *762*, 144194, doi:https://doi.org/10.1016/j.scitotenv.2020.144194.
564 Fu, Y., et al. (2022), Impact of Cloud Process in the Mixing State and Microphysical
565 Properties of Soot Particles: Implications in Light Absorption Enhancement [Dataset].
566 Zenodo, https://doi.org/10.5281/zenodo.4265639.
567 Gong, D., et al. (2018), Low-level summertime isoprene observed at a forested
568 mountaintop site in southern China: implications for strong regional atmospheric
569 oxidative capacity, *Atmospheric Chemistry and Physics*, *18*(19), 14417-14432,
570 doi:10.5194/acp-18-14417-2018.
571 Guo, S., M. Hu, Y. Lin, M. Gomez-Hernandez, M. L. Zamora, J. Peng, D. R. Collins,
572 and R. Zhang (2016), OH-Initiated Oxidation of m-Xylene on Black Carbon Aging,
573 *Environmental Science & Technology*, *50*(16), 8605-8612,
574 doi:10.1021/acs.est.6b01272.
575 Healy, R. M., et al. (2015), Light-absorbing properties of ambient black carbon and

576 brown carbon from fossil fuel and biomass burning sources, *Journal of Geophysical*
577 *Research-Atmospheres*, *120*(13), 6619-6633, doi:10.1002/2015jd023382.
578 Jacobson, M. Z. (2001), Strong radiative heating due to the mixing state of black carbon
579 in atmospheric aerosols, *Nature*, *409*(6821), 695-697, doi:10.1038/35055518.
580 Kelesidis, G. A., D. Neubauer, L.-S. Fan, U. Lohmann, and S. E. Pratsinis (2022),
581 Enhanced Light Absorption and Radiative Forcing by Black Carbon Agglomerates,
582 *Environmental Science & Technology*, *56*(12), 8610-8618, doi:10.1021/acs.est.2c00428.
583 Khalizov, A. F., R. Zhang, D. Zhang, H. Xue, J. Pagels, and P. H. McMurry (2009),
584 Formation of highly hygroscopic soot aerosols upon internal mixing with sulfuric acid
585 vapor, *Journal of Geophysical Research-Atmospheres*, *114*, D05208,
586 doi:10.1029/2008jd010595.
587 Kim, H., S. Collier, X. Ge, J. Xu, Y. Sun, W. Jiang, Y. Wang, P. Herckes, and Q. Zhang
588 (2019), Chemical processing of water-soluble species and formation of secondary
589 organic aerosol in fogs, *Atmospheric Environment*, *200*, 158-166,
590 doi:10.1016/j.atmosenv.2018.11.062.
591 King, M. D., S. Platnick, W. P. Menzel, S. A. Ackerman, and P. A. Hubanks (2013),
592 Spatial and Temporal Distribution of Clouds Observed by MODIS Onboard the Terra
593 and Aqua Satellites, *Ieee Transactions on Geoscience and Remote Sensing*, *51*(7),
594 3826-3852, doi:10.1109/tgrs.2012.2227333.
595 Kupiszewski, P., et al. (2016), Ice residual properties in mixed-phase clouds at the high-
596 alpine Jungfraujoch site, *Journal of Geophysical Research-Atmospheres*, *121*(20),
597 12343-12362, doi:10.1002/2016jd024894.

598 Lack, D. A., and C. D. Cappa (2010), Impact of brown and clear carbon on light
599 absorption enhancement, single scatter albedo and absorption wavelength dependence
600 of black carbon, *Atmospheric Chemistry and Physics*, *10*(9), 4207-4220,
601 doi:10.5194/acp-10-4207-2010.
602 Lan, Z.-J., X.-F. Huang, K.-Y. Yu, T.-L. Sun, L.-W. Zeng, and M. Hu (2013), Light
603 absorption of black carbon aerosol and its enhancement by mixing state in an urban
604 atmosphere in South China, *Atmospheric Environment*, *69*, 118-123,
605 doi:10.1016/j.atmosenv.2012.12.009.
606 Li, K., X. Ye, H. Pang, X. Lu, H. Chen, X. Wang, X. Yang, J. Chen, and Y. Chen (2018),
607 Temporal variations in the hygroscopicity and mixing state of black carbon aerosols in
608 a polluted megacity area, *Atmospheric Chemistry and Physics*, *18*(20), 15201-15218,
609 doi:10.5194/acp-18-15201-2018.
610 Li, W., P. Li, G. Sun, S. Zhou, Q. Yuan, and W. Wang (2011), Cloud residues and
611 interstitial aerosols from non-precipitating clouds over an industrial and urban area in
612 northern China, *Atmospheric Environment*, *45*(15), 2488-2495,
613 doi:10.1016/j.atmosenv.2011.02.044.
614 Li, W., and L. Shao (2009), Transmission electron microscopy study of aerosol particles
615 from the brown hazes in northern China, *Journal of Geophysical Research-*
616 *Atmospheres*, *114*, D09302, doi:10.1029/2008jd011285.
617 Li, W., L. Shao, D. Zhang, C.-U. Ro, M. Hu, X. Bi, H. Geng, A. Matsuki, H. Niu, and
618 J. Chen (2016), A review of single aerosol particle studies in the atmosphere of East
619 Asia: morphology, mixing state, source, and heterogeneous reactions, *Journal of*

Cleaner Production, *112*, 1330-1349, doi:10.1016/j.jclepro.2015.04.050.

Lin, Q., et al. (2019), Enrichment of submicron sea-salt-containing particles in small cloud droplets based on single-particle mass spectrometry, *Atmospheric Chemistry and Physics*, *19*(16), 10469-10479, doi:10.5194/acp-19-10469-2019.

Liu, D., J. Allan, J. Whitehead, D. Young, M. Flynn, H. Coe, G. McFiggans, Z. L. Fleming, and B. Bandy (2013), Ambient black carbon particle hygroscopic properties controlled by mixing state and composition, *Atmospheric Chemistry and Physics*, *13*(4), 2015-2029, doi:10.5194/acp-13-2015-2013.

Liu, D., et al. (2017a), Black-carbon absorption enhancement in the atmosphere determined by particle mixing state, *Nature Geoscience*, *10*(3), 184-U132, doi:10.1038/ngeo2901.

Liu, L., et al. (2017b), Morphology, composition, and mixing state of primary particles from combustion sources - crop residue, wood, and solid waste, *Scientific Reports*, *7*, 5047, doi:10.1038/s41598-017-05357-2.

Liu, L., et al. (2018), Cloud scavenging of anthropogenic refractory particles at a mountain site in North China, *Atmospheric Chemistry and Physics*, *18*(19), 14681-14693, doi:10.5194/acp-18-14681-2018.

Liu, S., et al. (2015), Enhanced light absorption by mixed source black and brown carbon particles in UK winter, *Nature Communications*, *6*, 8435, doi:10.1038/ncomms9435.

Luo, J., Q. Zhang, J. Luo, J. Liu, Y. Huo, and Y. Zhang (2019), Optical Modeling of Black Carbon With Different Coating Materials: The Effect of Coating Configurations,

642 *Journal of Geophysical Research-Atmospheres*, *124*(23), 13230-13253,
643 doi:10.1029/2019jd031701.
644 Lv, S., et al. (2019), Elevated levels of glyoxal and methylglyoxal at a remote mountain
645 site in southern China: Prompt in-situ formation combined with strong regional
646 transport, *The Science of the total environment*, *672*, 869-882,
647 doi:10.1016/j.scitotenv.2019.04.020.
648 Ma, X., C. D. Zangmeister, J. Gigault, G. W. Mulholland, and M. R. Zachariah (2013),
649 Soot aggregate restructuring during water processing, *Journal of Aerosol Science*, *66*,
650 209-219, doi:10.1016/j.jaerosci.2013.08.001.
651 Mahrt, F., K. Kilchhofer, C. Marcolli, P. Gronquist, R. O. David, M. Rosch, U.
652 Lohmann, and Z. A. Kanji (2020), The Impact of Cloud Processing on the Ice
653 Nucleation Abilities of Soot Particles at Cirrus Temperatures, *Journal of Geophysical*
654 *Research-Atmospheres*, *125*(3), e2019JD030922, doi:10.1029/2019jd030922.
655 Nakayama, T., Y. Ikeda, Y. Sawada, Y. Setoguchi, S. Ogawa, K. Kawana, M. Mochida,
656 F. Ikemori, K. Matsumoto, and Y. Matsumi (2014), Properties of light-absorbing
657 aerosols in the Nagoya urban area, Japan, in August 2011 and January 2012:
658 Contributions of brown carbon and lensing effect, *Journal of Geophysical Research-*
659 *Atmospheres*, *119*(22), 12721-12739, doi:10.1002/2014jd021744.
660 Nakayama, T., Y. Matsumi, K. Sato, T. Imamura, A. Yamazaki, and A. Uchiyama
661 (2010), Laboratory studies on optical properties of secondary organic aerosols
662 generated during the photooxidation of toluene and the ozonolysis of alpha-pinene,
663 *Journal of Geophysical Research-Atmospheres*, *115*, doi:10.1029/2010jd014387.

664 Nichman, L., M. Wolf, P. Davidovits, T. B. Onasch, Y. Zhang, D. R. Worsnop, J.
665 Bhandari, C. Mazzoleni, and D. J. Cziczo (2019), Laboratory study of the
666 heterogeneous ice nucleation on black-carbon-containing aerosol, *Atmospheric*
667 *Chemistry and Physics*, *19*(19), 12175-12194, doi:10.5194/acp-19-12175-2019.
668 NOAA. (2022). Hybrid single-particle Lagrangian integrated trajectory model
669 [Software]. NOAA. Retrieved from https://www.ready.noaa.gov/HYSPLIT.php.
670 Park, S. H., S. L. Gong, V. S. Bouchet, W. Gong, P. A. Makar, M. D. Moran, C. A.
671 Stroud, and J. Zhang (2011), Effects of black carbon aging on air quality predictions
672 and direct radiative forcing estimation, *Tellus Series B-Chemical and Physical*
673 *Meteorology*, *63*(5), 1026-1039, doi:10.1111/j.1600-0889.2011.00558.x.
674 Peng, J., et al. (2016), Markedly enhanced absorption and direct radiative forcing of
675 black carbon under polluted urban environments, *Proceedings of the National Academy*
676 *of Sciences of the United States of America*, *113*(16), 4266-4271,
677 doi:10.1073/pnas.1602310113.
678 Penner, J. E., J. Quaas, T. Storelvmo, T. Takemura, O. Boucher, H. Guo, A. Kirkevag,
679 J. E. Kristjansson, and O. Seland (2006), Model intercomparison of indirect aerosol
680 effects, *Atmospheric Chemistry and Physics*, *6*, 3391-3405, doi:10.5194/acp-6-3391-
681 2006.
682 Pratt, K. A., A. J. Heymsfield, C. H. Twohy, S. M. Murphy, P. J. DeMott, J. G. Hudson,
683 R. Subramanian, Z. Wang, J. H. Seinfeld, and K. A. Prather (2010), In Situ Chemical
684 Characterization of Aged Biomass-Burning Aerosols Impacting Cold Wave Clouds,
685 *Journal of the Atmospheric Sciences*, *67*(8), 2451-2468, doi:10.1175/2010jas3330.1.

686 Qiu, C., A. F. Khalizov, and R. Zhang (2012), Soot Aging from OH-Initiated Oxidation
687 of Toluene, *Environmental Science & Technology*, *46*(17), 9464-9472,
688 doi:10.1021/es301883y.
689 Radney, J. G., R. You, X. Ma, J. M. Conny, M. R. Zachariah, J. T. Hodges, and C. D.
690 Zangmeister (2014), Dependence of Soot Optical Properties on Particle Morphology:
691 Measurements and Model Comparisons, *Environmental Science & Technology*, *48*(6),
692 3169-3176, doi:10.1021/es4041804.
693 Samson, R. J., G. W. Mulholland, and J. W. Gentry (1987), STRUCTURAL-
694 ANALYSIS OF SOOT AGGLOMERATES, *Langmuir*, *3*(2), 272-281,
695 doi:10.1021/la00074a022.
696 Scarnato, B. V., S. Vahidinia, D. T. Richard, and T. W. Kirchstetter (2013), Effects of
697 internal mixing and aggregate morphology on optical properties of black carbon using
698 a discrete dipole approximation model, *Atmospheric Chemistry and Physics*, *13*(10),
699 5089-5101, doi:10.5194/acp-13-5089-2013.
700 Schnaiter, M., H. Horvath, O. Mohler, K. H. Naumann, H. Saathoff, and O. W. Schock
701 (2003), UV-VIS-NIR spectral optical properties of soot and soot-containing aerosols,
702 *Journal of Aerosol Science*, *34*(10), 1421-1444, doi:10.1016/s0021-8502(03)00361-6.
703 Schnaiter, M., C. Linke, O. Mohler, K. H. Naumann, H. Saathoff, R. Wagner, U.
704 Schurath, and B. Wehner (2005), Absorption amplification of black carbon internally
705 mixed with secondary organic aerosol, *Journal of Geophysical Research-Atmospheres*,
706 *110*(D19), D19204, doi:10.1029/2005jd006046.
707 Schneider, J., S. Mertes, D. van Pinxteren, H. Herrmann, and S. Borrmann (2017),

708 Uptake of nitric acid, ammonia, and organics in orographic clouds: mass spectrometric
709 analyses of droplet residual and interstitial aerosol particles, *Atmospheric Chemistry*
710 *and Physics*, *17*(2), 1571-1593, doi:10.5194/acp-17-1571-2017.
711 Schnitzler, E. G., J. M. Gac, and W. Jaeger (2017), Coating surface tension dependence
712 of soot aggregate restructuring, *Journal of Aerosol Science*, *106*, 43-55,
713 doi:10.1016/j.jaerosci.2017.01.005.
714 Sharma, N., S. China, J. Bhandari, K. Gorkowski, M. Dubey, R. A. Zaveri, and C.
715 Mazzoleni (2018), Physical Properties of Aerosol Internally Mixed With Soot Particles
716 in a Biogenically Dominated Environment in California, *Geophysical Research Letters*,
717 *45*(20), 11473-11482, doi:10.1029/2018gl079404.
718 Shingler, T., et al. (2012), Characterisation and airborne deployment of a new
719 counterflow virtual impactor inlet, *Atmospheric Measurement Techniques*, *5*(6), 1259-
720 1269, doi:10.5194/amt-5-1259-2012.
721 Shiraiwa, M., A. Zuend, A. K. Bertram, and J. H. Seinfeld (2013), Gas-particle
722 partitioning of atmospheric aerosols: interplay of physical state, non-ideal mixing and
723 morphology, *Physical Chemistry Chemical Physics*, *15*(27), 11441-11453,
724 doi:10.1039/c3cp51595h.
725 Wang, Y., et al. (2021a), Nonlinear Enhancement of Radiative Absorption by Black
726 Carbon in Response to Particle Mixing Structure, *Geophysical Research Letters*, *48*(24),
727 doi:10.1029/2021gl096437.
728 Wang, Y., F. Liu, C. He, L. Bi, T. Cheng, Z. Wang, H. Zhang, X. Zhang, Z. Shi, and W.
729 Li (2017), Fractal Dimensions and Mixing Structures of Soot Particles during

730 Atmospheric Processing, *Environmental Science & Technology Letters*, *4*(11), 487-493,
731 doi:10.1021/acs.estlett.7b00418.
732 Wang, Y., Y. Pang, J. Huang, L. Bi, H. Che, X. Zhang, and W. Li (2021b), Constructing
733 Shapes and Mixing Structures of Black Carbon Particles With Applications to Optical
734 Calculations, *Journal of Geophysical Research-Atmospheres*, *126*(10),
735 e2021JD034620, doi:10.1029/2021jd034620. [Software].
736 Wang, Y., et al. (2021c), Unexpected seasonal variations and high levels of ozone
737 observed at the summit of Nanling Mountains: Impact of Asian monsoon on southern
738 China, *Atmospheric Environment*, *253*, doi:10.1016/j.atmosenv.2021.118378.
739 Wentzel, M., H. Gorzawski, K. H. Naumann, H. Saathoff, and S. Weinbruch (2003),
740 Transmission electron microscopical and aerosol dynamical characterization of soot
741 aerosols, *Journal of Aerosol Science*, *34*(10), 1347-1370, doi:10.1016/s0021-
742 8502(03)00360-4.
743 Worringen, A., M. Ebert, T. Trautmann, S. Weinbruch, and G. Helas (2008), Optical
744 properties of internally mixed ammonium sulfate and soot particles-a study of
745 individual aerosol particles and ambient aerosol populations, *Applied Optics*, *47*(21),
746 3835-3845, doi:10.1364/ao.47.003835.
747 Wu, Y., T. Cheng, D. Liu, J. D. Allan, L. Zheng, and H. Chen (2018), Light Absorption
748 Enhancement of Black Carbon Aerosol Constrained by Particle Morphology,
749 *Environmental Science & Technology*, *52*(12), 6912-6919,
750 doi:10.1021/acs.est.8b00636.
751 Xu, L., et al. (2020), Tracing the evolution of morphology and mixing state of soot

752 particles along with the movement of an Asian dust storm, *Atmospheric Chemistry and*
753 *Physics*, *20*(22), 14321-14332, doi:10.5194/acp-20-14321-2020.
754 Yang, Y., et al. (2021), Stage-resolved in-cloud scavenging of submicron and BC-
755 containing particles: A case study, *Atmospheric Environment*, *244*,
756 doi:10.1016/j.atmosenv.2020.117883.
757 Yu, H., W. Li, Y. Zhang, P. Tunved, M. Dall'Osto, X. Shen, J. Sun, X. Zhang, J. Zhang,
758 and Z. Shi (2019), Organic coating on sulfate and soot particles during late summer in
759 the Svalbard Archipelago, *Atmospheric Chemistry and Physics*, *19*(15), 10433-10446,
760 doi:10.5194/acp-19-10433-2019.
761 Yuan, Q., J. Xu, Y. Wang, X. Zhang, Y. Pang, L. Liu, L. Bi, S. Kang, and W. Li (2019),
762 Mixing State and Fractal Dimension of Soot Particles at a Remote Site in the
763 Southeastern Tibetan Plateau, *Environmental Science & Technology*, *53*(14), 8227-
764 8234, doi:10.1021/acs.est.9b01917.
765 Zelenyuk, A., D. Imre, M. Earle, R. Easter, A. Korolev, R. Leaitch, P. Liu, A. M.
766 Macdonald, M. Ovchinnikov, and W. Strapp (2010), In Situ Characterization of Cloud
767 Condensation Nuclei, Interstitial, and Background Particles Using the Single Particle
768 Mass Spectrometer, SPLAT II, *Analytical Chemistry*, *82*(19), 7943-7951,
769 doi:10.1021/ac1013892.
770 Zhang, G., et al. (2017a), The single-particle mixing state and cloud scavenging of
771 black carbon: a case study at a high-altitude mountain site in southern China,
772 *Atmospheric Chemistry and Physics*, *17*(24), 14975-14985, doi:10.5194/acp-17-14975-
773 2017.

774 Zhang, G., et al. (2017b), Insight into the in-cloud formation of oxalate based on in situ
775 measurement by single particle mass spectrometry, *Atmospheric Chemistry and Physics*,
776 *17*(22), 13891-13901, doi:10.5194/acp-17-13891-2017.
777 Zhang, H., H. Guo, J. Hu, Q. Ying, and M. J. Kleemani (2019), Modeling Atmospheric
778 Age Distribution of Elemental Carbon Using a Regional Age-Resolved Particle
779 Representation Framework, *Environmental Science & Technology*, *53*(1), 270-278,
780 doi:10.1021/acs.est.8b05895.
781 Zhang, R., A. F. Khalizov, J. Pagels, D. Zhang, H. Xue, and P. H. McMurry (2008),
782 Variability in morphology, hygroscopicity, and optical properties of soot aerosols
783 during atmospheric processing, *Proceedings of the National Academy of Sciences of the*
784 *United States of America*, *105*(30), 10291-10296, doi:10.1073/pnas.0804860105.
785 Zhang, X., and M. Mao (2020), Radiative properties of coated black carbon aerosols
786 impacted by their microphysics, *Journal of Quantitative Spectroscopy & Radiative*
787 *Transfer*, *241*, 106718, doi:10.1016/j.jqsrt.2019.106718.
788 Zhang, Y., et al. (2018), Direct Observations of Fine Primary Particles From Residential
789 Coal Burning: Insights Into Their Morphology, Composition, and Hygroscopicity,
790 *Journal of Geophysical Research-Atmospheres*, *123*(22), 12964-12979,
791 doi:10.1029/2018jd028988.
792 Zhuang, B. L., L. Liu, F. H. Shen, T. J. Wang, and Y. Han (2010), Semidirect radiative
793 forcing of internal mixed black carbon cloud droplet and its regional climatic effect
794 over China, *Journal of Geophysical Research-Atmospheres*, *115*,
795 doi:10.1029/2009jd013165.

References From the Supporting Information

Brasil, A. M., T. L. Farias, and M. G. Carvalho (1999), A recipe for image characterization of fractal-like aggregates, *Journal of Aerosol Science*, *30*(10), 1379-1389, doi:10.1016/s0021-8502(99)00026-9.

Oh, C., and C. M. Sorensen (1997), The effect of overlap between monomers on the determination of fractal cluster morphology, *Journal of Colloid and Interface Science*, *193*(1), 17-25, doi:10.1006/jcis.1997.5046.

Figure1.

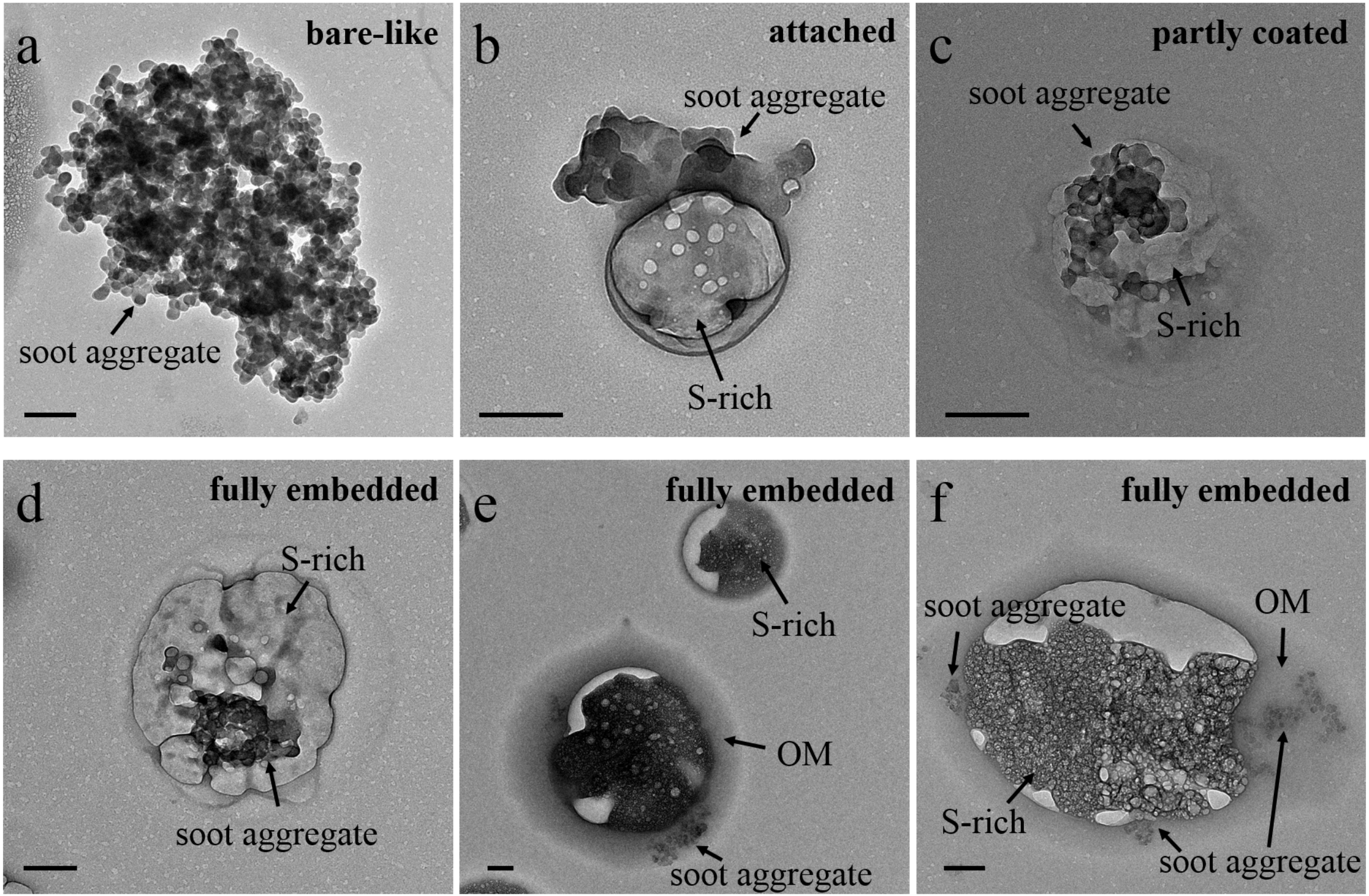
a
bare-like
soot aggregate
b
attached
soot aggregate
S-rich
c
partly coated
soot aggregate
S-rich
d
fully embedded
S-rich
soot aggregate
e
fully embedded
S-rich
OM
soot aggregate
f
fully embedded
soot aggregate
OM
S-rich
soot aggregate

Figure2.

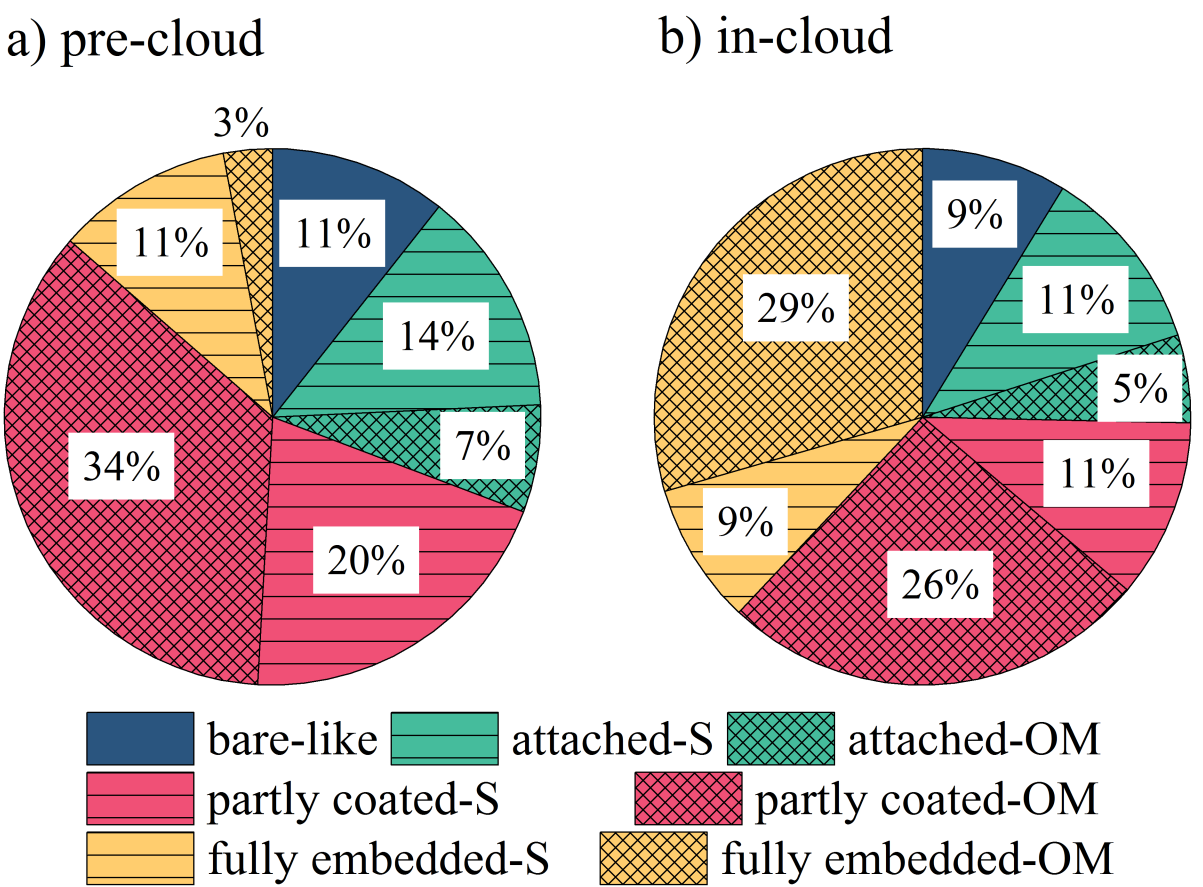
a) pre-cloud
3%
11%
11%
14%
7%
34%
20%
b) in-cloud
9%
11%
29%
5%
11%
9%
26%
bare-like
attached-S
attached-OM
partly coated-S
partly coated-OM
fully embedded-S
fully embedded-OM

Figure3.

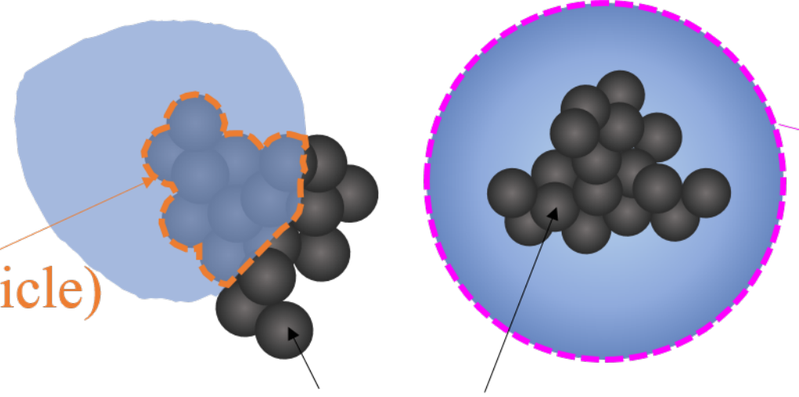

A_{coated} (the projected area of soot aggregate embedded in the host particle)

A_p (the projected area of particle)

A_a (the projected area of soot aggregate)

a)

$F = \frac{A_{coated}}{A_a}$

b)

pre-cloud

in-cloud

$D_p/D_c = \frac{\sqrt{A_p}}{\sqrt{A_a}}$

normalized particle number

F

Dp/Dc

Figure4.

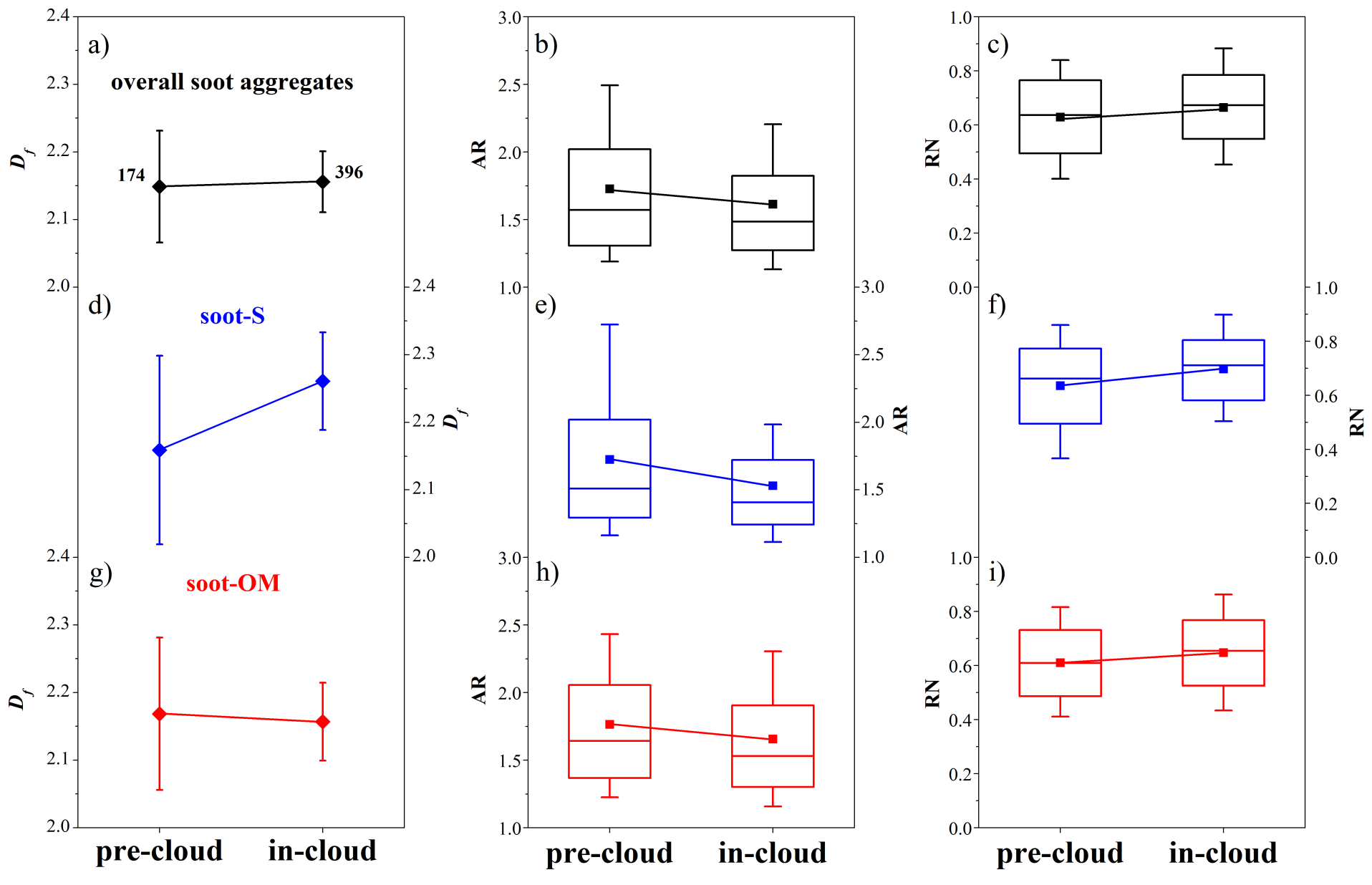
a)
overall soot aggregates
174
396
d)
soot-S
g)
soot-OM
b)
e)
h)
c)
f)
i)
D_f
AR
RN
pre-cloud
in-cloud

Figure5.

a) soot particle with partly coated structure

b) soot particle with fully embedded structure

Eabs

Dp/Dc

soot-S of pre-cloud period
soot-OM of pre-cloud period
soot-S of in-cloud period
soot-OM of in-cloud period

c) shape models

bare-like

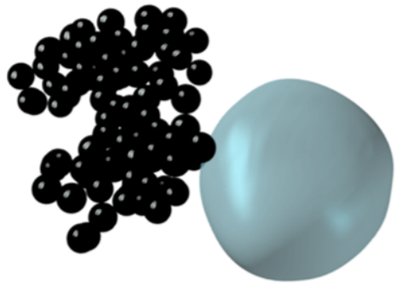

attached

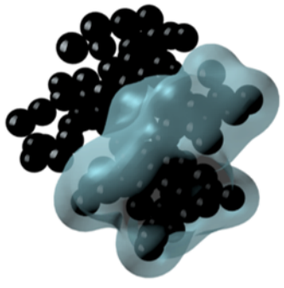

partly coated

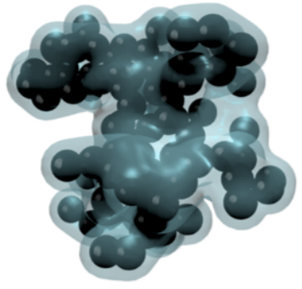

fully embedded

d) overall soot particles

pre-cloud period
in-cloud period

Eabs

Dp/Dc

Figure6.

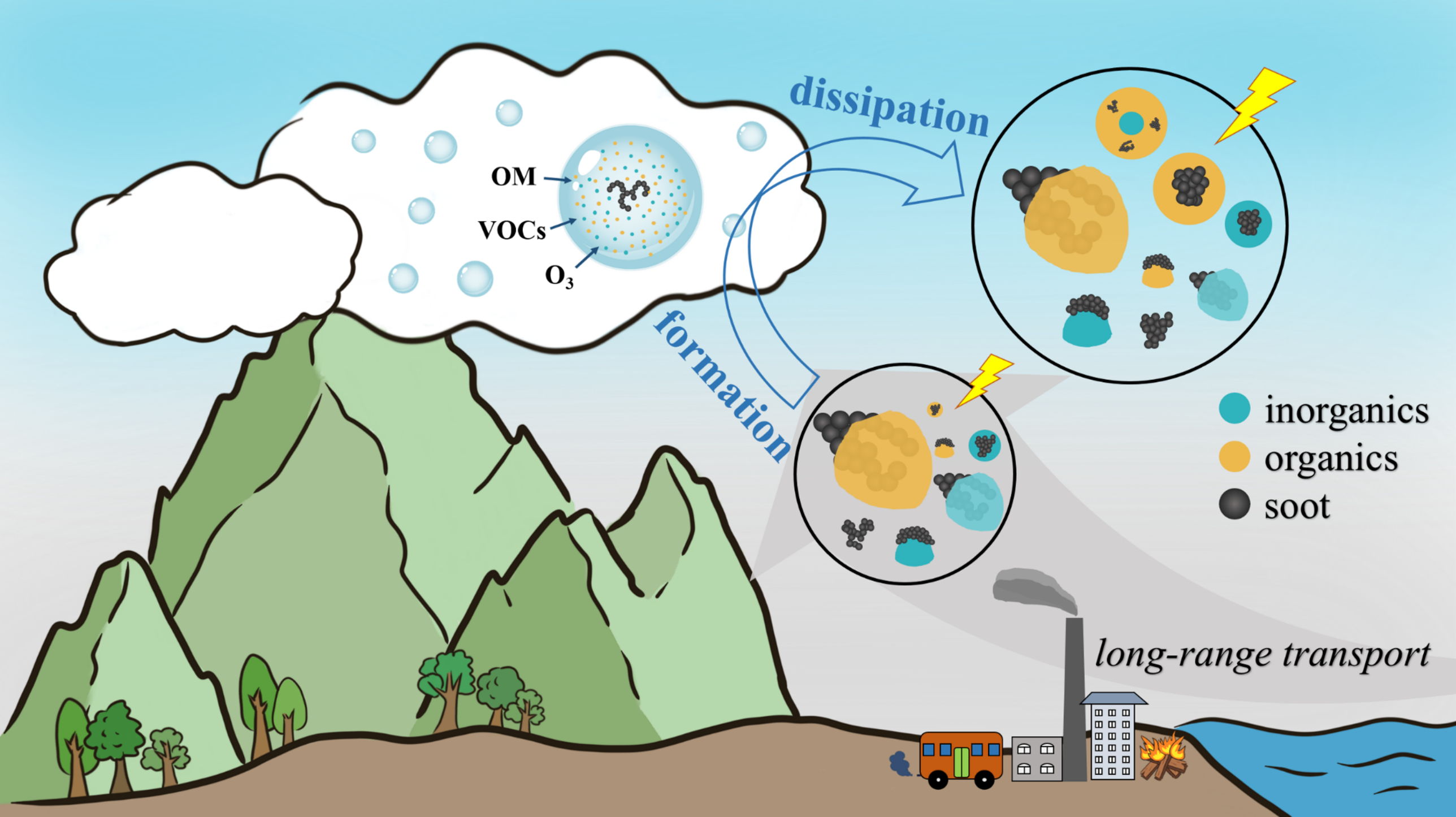
dissipation
formation
OM
VOCs
O_3
inorganics
organics
soot
long-range transport